

APPENDIX D: COUPON TESTING

Wind turbines offer a sustainable and clean source of electricity. Because the energy that can be converted into electrical energy increases with the square of the blade length, the lengths of the utility-scale wind turbine blades have significantly increased over the past two decades seen in Figure D-1 [1]. As blade lengths increase so do the loads on the blades resulting from the wind and from the axial forces due to spinning. Continuous fiber-reinforced composite fabrics are the material of choice for the manufacture of the blades with the objective of keeping blade mass at a minimum by taking advantage of the high strength-to-weight and stiffness-to-weight ratios of composites.

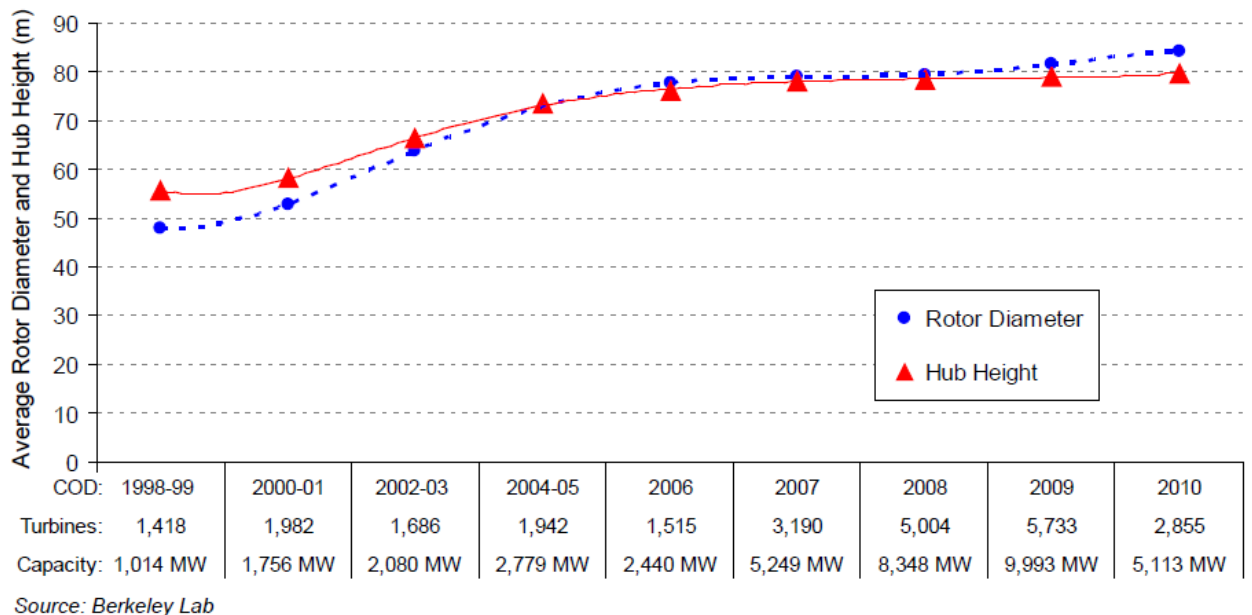


Figure D-1. Average rotor diameter vs. time [1]

To keep the cost of wind energy competitive with fossil fuels, blade manufacturers are motivated to use relatively inexpensive fabrication processes. The manufacturing of strength-driven designs with low-cost processes such as hand lay-up and resin transfer molding can lead to defects that compromise the overall structural behavior of the blades. These defects are typically in the form of out-of-plane waves and can be due to either poor hand lay-up or layers of fabric bunching together during the vacuum compaction of the fabric plies. Subsequently, these waves may either fold onto adjacent layers to create wrinkles, or the area beneath the waves can be resin-rich pockets, creating a potential weak spot at that location along the blade shown in Figure D-2 [2].

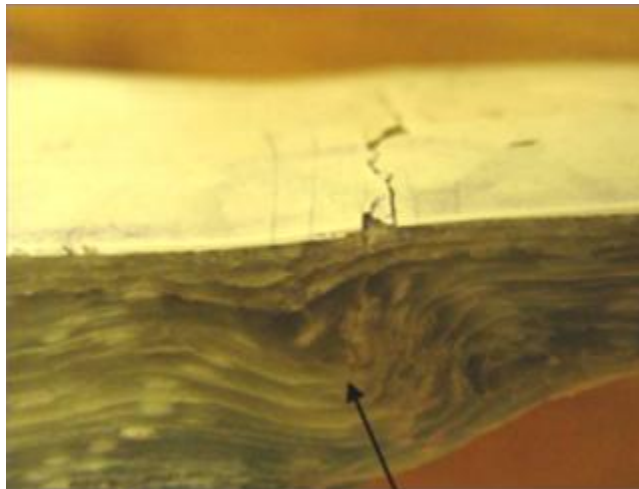


Figure D-2. Typical out-of-plane wave defect in a wind turbine blade [2]

In an effort to compensate for the presence of these manufacturing-induced wave defects, blade designers and manufacturers typically overdesign their blades, unnecessarily increasing weight and material costs. To improve designs, research efforts are focused on understanding these wave defects and other parameters that influence

blade performance and reliability [3-10]. These studies have shown that the existence of wave defects in coupon specimens increases the potential for a buckling mode of failure. Furthermore, the load path of the fibers is redirected from their intended orientation in the primary load direction, thus leading to matrix-dominated failures.

In the current study, glass-fiber/epoxy coupons are fabricated with wave defects and subsequently tested to measure the reduction in compressive strength and fatigue life relative to wave-defect free coupons as a result of wave defect through-thickness location, wave amplitude, and wave aspect ratio (wave length/wave amplitude). Pre-cured epoxy-only wave defects with controlled dimensions are inserted into various coupon samples shown in Figure D-3. Additionally, a nine-meter turbine blade is manufactured with pre-cured, controlled wave defects in prescribed locations along the spar cap and then cut into test coupons. The subsequent sections of this paper describe the coupon fabrication process, experimental parameters, and the results of the static and fatigue tests. Three-dimensional Digital Image Correlation (3D DIC) measurements and finite element (FE) models are used for data comparison and interpretation purposes. The results of this study provide insight on the impact of wave defects on the structural integrity as observed in the associated strain amplification in the region surrounding the defect of composite wind turbine blades and other structures made using a similar manufacturing process.

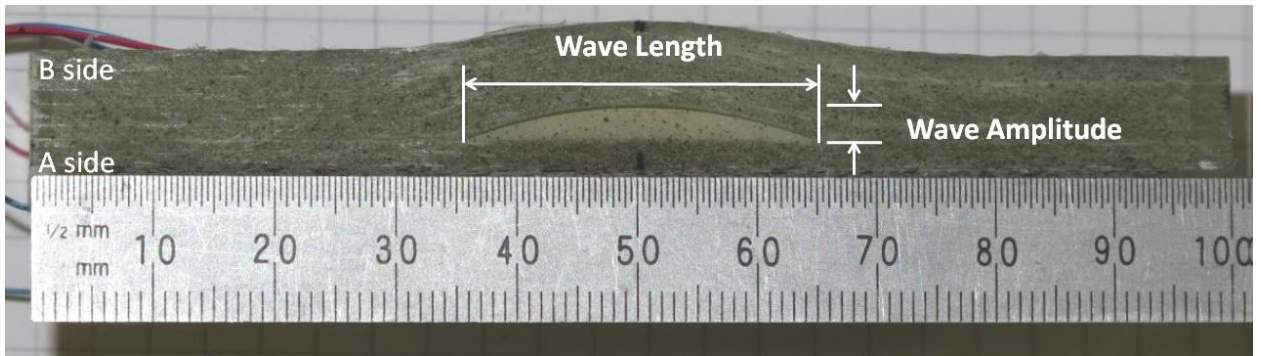


Figure D-3. Example of coupon with wave defect dimensions.

1 Materials and Experiments

The following sections describe the materials used in this study, and the methods used to fabricate the various test specimens. In addition, the experimental setup and test parameters are described.

1.1 Materials and fabrication

The nine-meter wind turbine blade and two sets of test specimens were fabricated at TPI Composites in Warren, RI (USA). The blade and the materials used to fabricate the two sets of coupon specimens were based on the design of the Sandia National Laboratories (SNL) research blade (Model CX-100) [11]. Each set was made using a ply stack of non-crimp fabric (NCF) made by Vectorply Corporation and infused with resin using a vacuum bag process. The two sets of coupons were fabricated using a biaxial E-glass NCF referred to as E-LT 5500. The first set of coupons (104-mm long x 40-mm wide x 20-mm thick) was fabricated using 16 layers. The second set (104-mm long x 40-mm wide x 10-mm thick) was fabricated with eight layers of fabric to be more representative of section thicknesses in the CX-100 blade. In each set of samples, the

dimensions were chosen based on ASTM Standard D695-10 for defect-free samples such that failure would occur prior to buckling. A third set of specimens was cut from the spar cap of the CX-100 blade which is comprised of a E-glass double-bias NCF referred to as E-BX 0900 and a unidirectional carbon NCF referred to as C-LA 2012. The properties of the NCFs and of the epoxy resin are summarized in Tables D-1 and D-2, respectively.

Table D-1. Properties of Vectorply Non-Crimp Fabrics

Manufacturer's style	E-LT 5500	E-BX 0900	C-LA 2012
Architecture	0°/90° Biaxial NCF	+/-45° Double Bias NCF	0° Unidirectional NCF
Fiber Type	E-Glass	E-Glass	Carbon
Area Density [g/m ²]	1842.2	334	710
Thickness [mm]	1.45	0.31	1.12
Elastic Modulus [GPa]	60.6	60.6	126.6

Table D-2. Cured Properties of HEXION RIMR 135 Epoxy

Manufacturer's style	RIMR 135
Resin Type	Epoxy
Density [g/cm ³]	1.13 - 1.17
Elastic Modulus [GPa]	1.6

The wave defects embedded within the coupon specimens were characterized by wave length and amplitude, as well as by through-thickness location shown in Figure D-3. The through-thickness location of the defect was defined as being near the A-side (closest to the mold), in the middle, or near to the B-side (furthest from the mold). The

amplitudes of the wave defects were 1, 2, and 3 mm. The aspect ratios were 5, 10, and 15. The dimensions of the wave defects were controlled by pouring epoxy into a mold with channels corresponding to various wave amplitudes and aspect ratios seen in Figure D-4. Once cured, the defects were removed from the mold and inserted at various through-thickness locations in each laminate. A minimum of five samples for each configuration was fabricated and tested to explore repeatability.

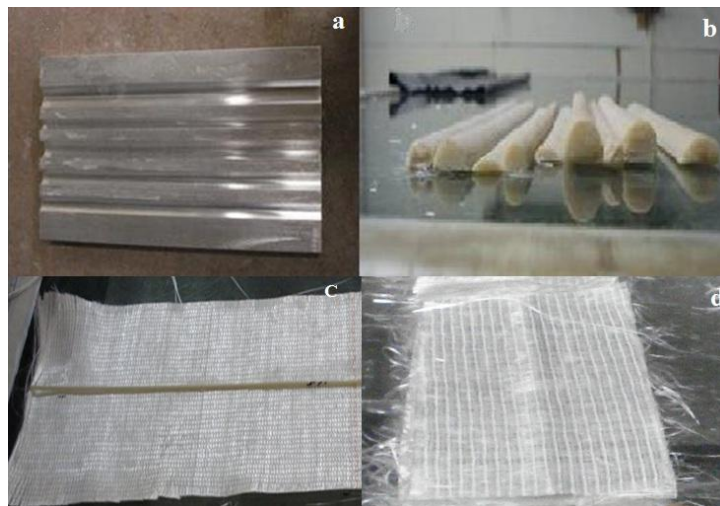


Figure D-4 (a) Resin rod mold; (b) resin rods of various aspect ratios fabricated using mold; (c) example of layup and (d) example of rod and fabric layers to create controlled wave defect

In the first set of coupons (20-mm thick), defect-free samples were also fabricated to establish a reference, i.e. a baseline, to which all other samples could be compared. The first set of compression-test configurations is shown in Table D-3. Note that the wave height was held constant (3 mm) for this set, and the effects of aspect ratio and through-thickness location on compressive strength were studied.

Table D-3. Compression-test matrix for first set of coupons

Sample Configuration No.	Defect Amplitude (mm)	Defect Length (mm)	Defect Location
1 (Reference)	0	0	None
2	3	15	A-side
3		30	
4		45	
5		15	Middle
6		30	
7		45	
8		15	B-side
9		30	
10		45	

The intent of the second set of coupons (10-mm thick) was to isolate the effect of wave amplitude on compressive strength. Therefore, as shown in Table D-4, the wave defects were fabricated with a constant aspect ratio of 10, and were embedded in the middle of the coupons to keep the through-thickness location constant.

Table D-4. Compression-test matrix for second set of coupons

Sample Configuration No.	Defect Amplitude (mm)	Defect Length (mm)	Defect Location
1	1	10	Middle
2	2	20	
3	3	30	

The third set of test coupons was comprised of wave defects with a fixed 3-mm amplitude that had been embedded within the spar cap of the CX-100 blade at the 3.5, 5.0, and 6.0-m span-wise locations (measured from the blade root). The defects at the

3.5-m location had an aspect ratio of 15, while the defects at the 5.0- and 6.0-m locations had aspect ratios of 10 and 5, respectively. The third set of coupons was cut from these three spar cap locations to create specimens for fatigue tests. Defect-free coupons were also cut from the areas surrounding the three defects. Static tests were first performed on some specimens from this the third set of coupons to measure maximum failure loads, which were used as the basis for assigning the magnitude of the fatigue test loads. Table D-5 summarizes the third set of coupons. The sample nomenclature is as follows: span location in meters, high (HP) or low pressure (LP) side, number of plies, defect present (D) or not (N), and sample number, e.g. sample 5.0HP3D-1 consists of sample number 1 taken from the 5.0-m span location on the high pressure side with three plies of carbon fabric (C-LA 2012) and a defect.

Table D-5. Test matrix for third set of coupons

Sample		Defect Amplitude (mm)	Defect Aspect Ratio
LP	HP		
3.4LP3N-1	3.4HP3N-1	0	0
3.4LP3N-2	3.4HP3N-2		
3.4LP3N-3	3.4HP3N-3		
3.4LP3N-4	3.4HP3N-4		
3.5LP3D-1	3.5HP3D-1	3	15
3.5LP3D-2	3.5HP3D-2		
3.5LP3D-3	3.5HP3D-3		
3.5LP3D-4	3.5HP3D-4		
3.6LP3N-1	3.6HP3N-1	0	0
3.6LP3N-2	3.6HP3N-2		
3.6LP3N-3	3.6HP3N-3		
3.6LP3N-4	3.6HP3N-4		
4.9LP3N-1	4.9HP3N-1	0	0
4.9LP3N-2	4.9HP3N-2		
4.9LP3N-3	4.9HP3N-3		
5.0LP3D-1	5.0HP3D-1	3	10
5.0LP3D-2	5.0HP3D-2		
5.0LP3D-3	5.0HP3D-3		
5.1LP3N-1	5.1HP3N-1	0	0
5.1LP3N-2	5.1HP3N-2		
5.1LP3N-3	5.1HP3N-3		
5.9LP3N-1	5.9HP3N-1	0	0
5.9LP3N-2	5.9HP3N-2		
6.0LP3D-1	6.0HP3D-1	3	5
6.0LP3D-2	6.0HP3D-2		
6.1LP3N-1	6.1HP3N-1	0	0
6.1LP3N-2	6.1HP3N-2		

1.2 Static experiments

This section is divided into three subsections. The first subsection describes the static compression test parameters used on all three sets of coupons. The second subsection describes tension-plug tests conducted to study the bond strength between the pre-cured epoxy defect and the adjacent plies. The third subsection outlines the fatigue-test parameters used on the third set of coupons.

1.2.1 Compression tests

A servo-hydraulic MTS 810 test station with a 409-kN load capacity was used to compress the test specimens with a crosshead displacement rate of 1 mm/min. One end of the sample was placed directly onto the bottom plate of the fixture, and other end of the sample was contacted by the top plate of the fixture to provide the compressive force. Figure D-5 shows the test configuration for the first set of samples, similar to test standard ISO 14126. This test configuration required that the samples be cut such that the ends were perfectly flat. The slightest imperfection in the cutting and placement of the samples resulted in a brooming-type failure (Figure D-6a), as the load was not evenly distributed across the cross-section. After observing brooming failures due to challenges with respect to the cutting of the first set of coupons, clamps were used at each end of the second and third sets of coupon specimens (Figure D-6b) with the objective of eliminating the brooming failure mode.



Figure D-5. Static compression test of sample 45x3A

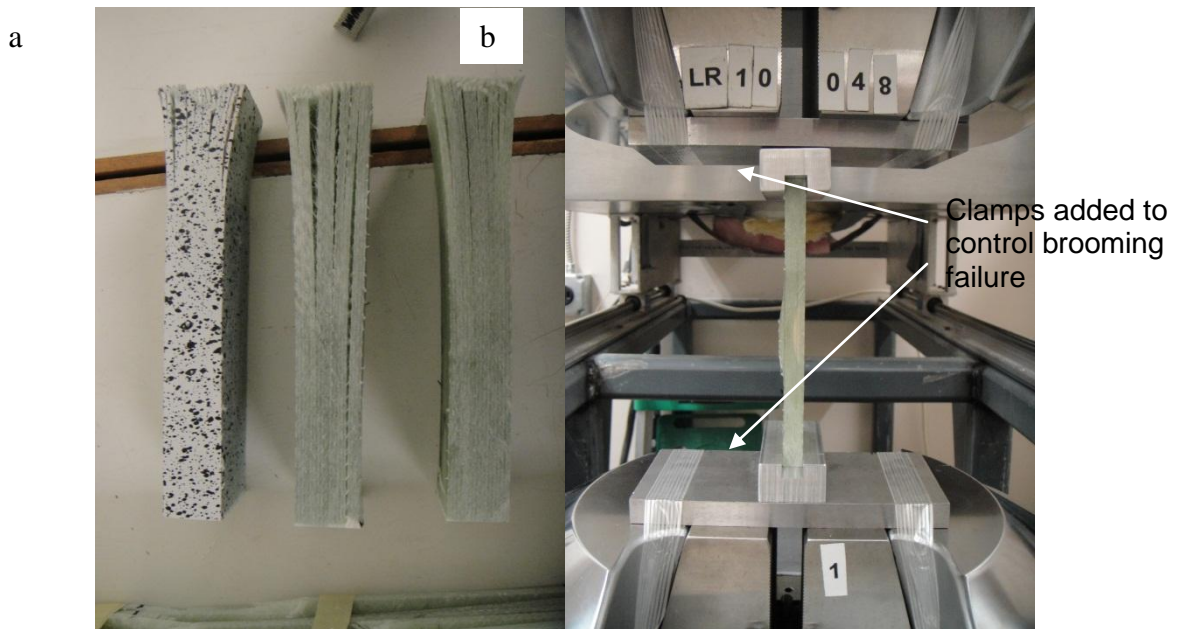


Figure D-6. (a) Baseline coupon samples that have failed due to brooming (speckled pattern required for DIC measurements); (b) the addition of clamps to prevent brooming failure

Three-dimensional DIC has recently emerged as an effective optical strain-measurement technique for structural health monitoring of wind turbine blades and the detection of defects [12, 13]. Thus, several of the tested samples were speckled with a dotted pattern such that DIC could be used to measure the strain field on the outer surface. The 3D DIC system (AramisTM), made by GOM, utilized a pair of cameras with Schneider Kreuznach Cinegon 1.4/12-0906 lenses and approximately 2 Mega-pixel resolution (1600 x 1200). The system was used to characterize the strain resulting from the presence of the controlled defects in the coupon samples by observing the amplification of strain on the outer surface.

Figure D-7 shows a typical 3D DIC measurement during static compression tests. The Epsilon Y strain vs. Section length plot shows the variation in the strain along the length of the test specimen. This plot shows the strain in the area of the wave defect to be more than double the nominal strain away from the defect. The Epsilon Y strain vs. Time plot shows the change in strain as a function of time up to the instant of specimen failure.

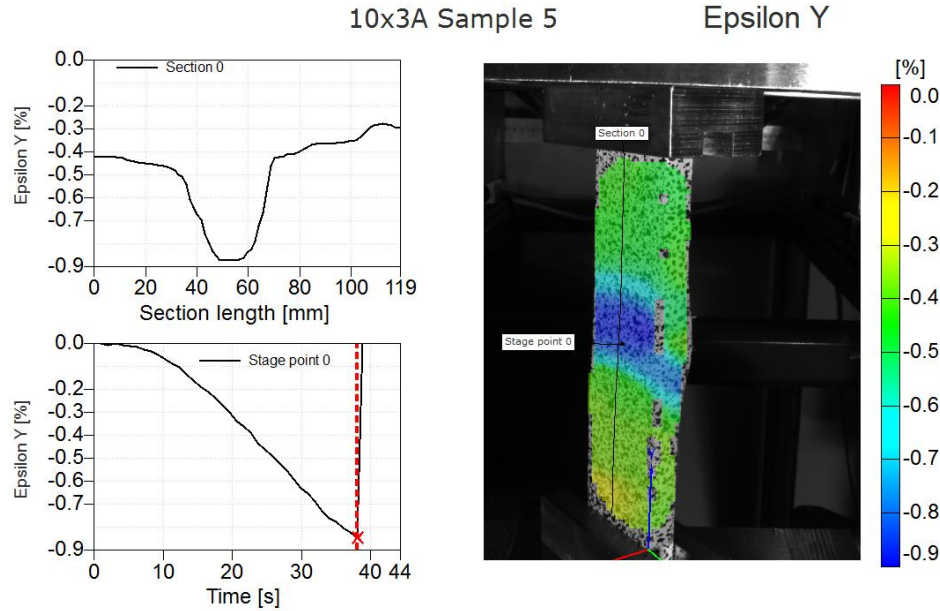


Figure D-7. Typical DIC measurement during static compression tests on coupon specimens

1.2.2 Interface bonding tests

The resulting wave length and amplitude of a manufacturing-induced wave defect in a wind turbine blade occur as a consequence of the combination of the fabric placement and subsequent epoxy infusion steps. Thus, the resulting wave length and amplitude are not necessarily well controlled by the process. To control the dimensions of the wave defects for the current study, the defects were pre-made with epoxy waves, inserted between layers of fabric, and the fabric-defect assembly was then infused with epoxy. In contrast to the actual manufacturing process where the defect results from a single-step infusion process, the test specimens required using a two-step infusion process. Thus, it was important to study the bond strength between the pre-infused defect and the rest of the laminate and compare that to the bond strength between a wave defect and the rest of the laminate resulting from a single-step infusion process. If the two-step

process resulted in a bond strength different from that occurring in the single-step process, then the credibility of the test results from the pre-cured defects would be compromised.

A tension-plug test was designed to compare the bond strength for specimens infused in a single step and with specimens infused in two separate steps (Figure D-8). As the samples are pulled uniaxially in tension, failure is expected to occur in the resin-rich area separating the layers of fabric, if the bond strength surrounding the defect is sufficient. If failure occurs at the interface between the fabric and the resin-rich area, then the failure might be a result of compromised bond strength between the defect and the rest of the laminate. Figure D-9 shows that failure occurred in the resin-rich section rather than at the interface between the resin and fabric. This phenomenon suggests that the bonding of the interface is not compromised and the test samples should fail as a result of the defect geometry rather than as a result of poor bonding.

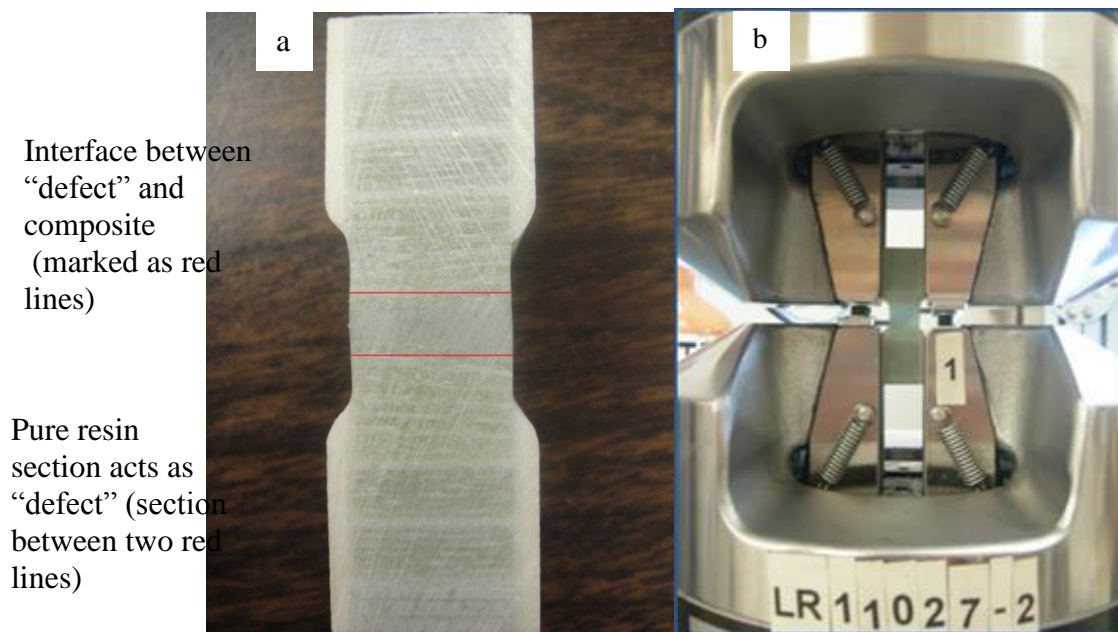


Figure D-8. (a) Bonding test sample and (b) set-up of tension-plug test

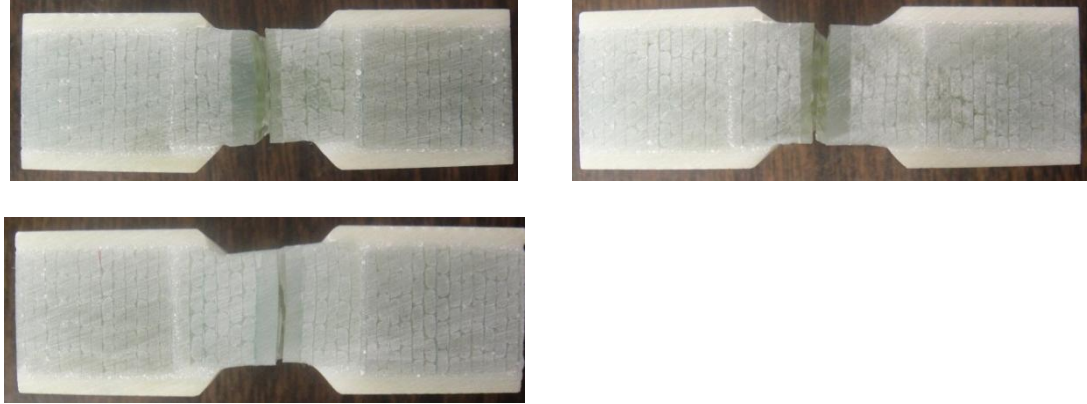


Figure D-9. Failure in samples during tension-plug tests

1.3 Fatigue tests

Fatigue tests on the third set of coupon samples were conducted on an MTS machine at SNL. The intent of these tests was to provide insight into the failure mechanism and any change in the number of cycles to failure of composite samples having defects that are loaded with an alternating compressive load. The samples were preloaded in compression and cycled from 3%-58% of the reference failure load for the first 65K cycles then 3%-81% of the reference failure load for the subsequent cycles. The reference failure load was determined from initial static tests on samples of the same configuration as the fatigue specimens. The static compression tests were performed to failure at a loading rate of 2.54 mm/min (0.1 in/min). The maximum load results are summarized in Table D-6.

Table D-6. Static test results of coupon samples cut from high pressure side of CX-100

Sample	Cross section of C-LA2012 (cm ²)	Max Load (kN)
3.6HP3N-2	1.13*	48.8
3.5HP3D-1		33.7
5.0HP3D-1		28.9
6.0HP3D-2		31.6

* Gel coat was not included in the area value because it does not contribute significantly to the load bearing capability of the coupon sample.

The lowest measured load of 28.9 kN was used as the reference failure load for the fatigue-test coupons. The maximum load for fatigue testing was concluded to be 16.8 kN (58% of reference failure loading) from 0 to 65,000 cycles; and 23.6 kN (81% of reference failure loading) from 65,001 to 85,000 cycles. Two conditions were run: fast cyclic loading and slow cyclic loading to enable DIC measurements to be taken. Fast cyclic loading was performed at a rate of 8 Hz with the objective of putting a large number of cycles on the sample. Slow loading performed at 0.5 Hz was to allow for the DIC cameras, limited to 12 frames per second, to capture 24 images per cycle.

2 Finite element modeling

Finite element models of the first and second sets of compression-test samples were generated to assist in the interpretation of the experimental results. A discrete, unit-cell approach was used to model the dry E-LT 5500 biaxial NCF and the deformation of this fabric during hand layup at the mesoscopic level. This mesoscopic-level model consists of four 1-D elements and one 2-D element. These five elements share a set of four nodes as shown in Figure D-10. The tensile and bending loads are carried by the 1-D beam elements, and these beams allow for the ability to track the changes in the

directions of the principal load carrying paths as a result of fabric deformation during a forming process. The 2-D shell element accounts only for the shearing resistance of the fabric and, hence, has no tensile stiffness. Details of the finite element modeling using this mesoscopic approach are available in [14, 15].

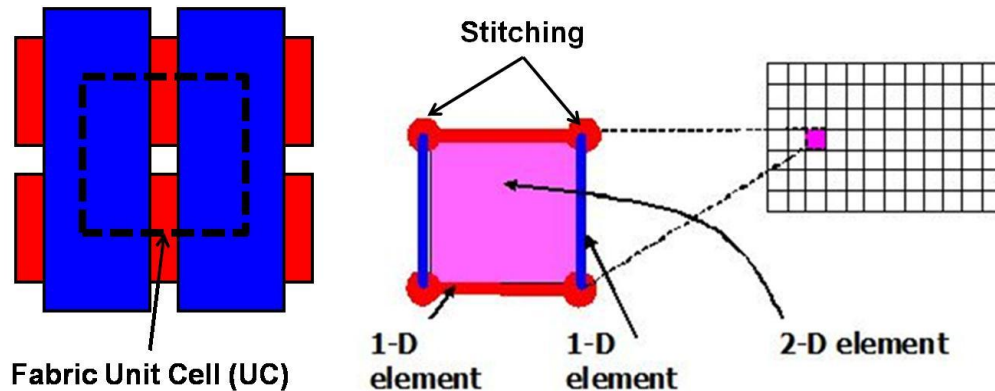


Figure D-10. Representative unit cell of the hybrid mesoscopic modeling of a biaxial NCF

As a first step in building the finite element models of the test coupons, wave defect inserts with the aspect ratios and amplitudes shown in Tables D-3 and D-4 were generated using eight-noded solid elements having the properties of the epoxy (Table D-2) so as to simulate the resin-rich pockets. These inserts were then placed within a set of fabric layers resting on a flat surface in such a position as to be in the middle, biased to the A-side, or biased to the B-side where the material behavior of the beams and shells used in the fabric meshes were prescribed to be those of the dry fabric. A pressure was applied to the fabric layers above the defect such that those layers could wrap around the defect, thereby simulating the forming of an out-of-plane wave defect within a composite laminate (Figure D-11). The properties of the beam and shell elements of the fabric layers were then changed to represent properties of a cured infused laminate. These cured

properties were determined through a series of static and dynamic mechanical tests on cured composite samples [16]. The multiple fabric layers are bonded together using tie constraints.

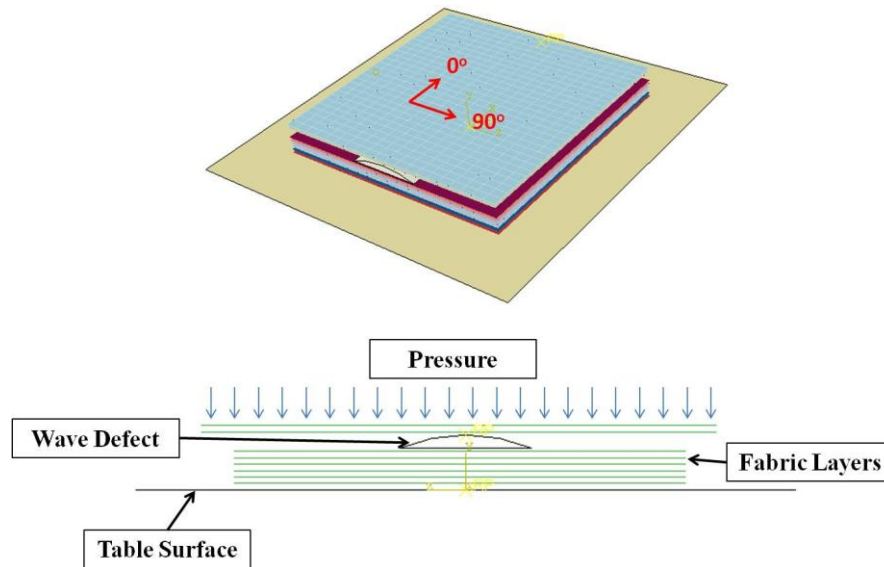


Figure D-11. Creating a compression test coupon model (biased to the B-side) in Abaqus

After all of the properties were assigned and the layers were bonded together, the finite element model of the laminate was “cut” into test coupons that were the same size as those tested in compression. The coupons were fixed at the bottom end, and a compressive displacement was prescribed at the top, representing the crosshead displacement.

Because the experimental baseline samples had failed prematurely due to brooming, it was not possible to compare the maximum compressive stress with the baseline finite element model quantitatively. Furthermore, the finite element models did not include failure criteria to capture matrix cracking and/or delamination and were therefore expected to yield higher maximum stresses than those measured

experimentally. Therefore, the distribution of the strains within the finite element models and the experimental test coupons were qualitatively compared. All compressive loads from the samples with wave defects were presented as a percentage of the baseline values. The maximum load from the coupon finite element models with wave defects was taken at the point at which the maximum strain from the baseline model (0.33%) was reached.

3 Results and Discussion

This section discusses the results from the static compression tests of the first and second sets of coupons, as well as from the fatigue tests. DIC measurements and finite element models are presented to support the experimental results.

3.1 Static compression tests

In-plane and/or out-of-plane fiber waviness is expected to reduce the compressive strength of composite materials [17-24]. As mentioned previously, this study focused on the effect of out-of-plane wave defects on compressive strength. In particular, the wave defect through-thickness location, amplitude and aspect ratio were varied to identify the critical defect parameters that significantly influence the laminate compressive strength.

The mean maximum compressive stress for the first set of coupons with configurations cited in Table D-3 as a function of aspect ratio and through-thickness location are summarized in Figure D-12. The error bars denote one standard deviation. The labels on the horizontal axis denote the wave defect aspect ratio and the defect

location. For example, sample “5A” refers to a sample with a wave defect aspect ratio of 5 that is located such that it is biased away from the middle toward the A-side of the specimen, as denoted in Figure D-2. Similarly, “B” refers to a B-side biased location and “M” refers to a defect embedded in the middle of the sample. The results consistently show that for the same wave defect amplitude (3 mm), the specimens with defects located close to the A-side were significantly weaker than specimens with defects either in the middle location or close to the B-side. The samples with defects located along the A-side were the weakest in compression because more layers of fabric were buckled out-of-plane to allow the fabric layers to conform to the wave defect than with the middle or B-side samples. While Figure D-12 indicates that the through-thickness location of a wave defect influences the compressive strength of a composite, the aspect ratio does not significantly impact the compressive strength. Also note that the failure of the baseline sample was premature as a result of brooming, as was previously shown in Figure D-6. Recall that end clamps were used to prevent brooming for the subsequent testing of the embedded-defect samples. Thus, had such clamps been used in the testing of the baseline test coupons, it is anticipated that the failure strength would be greater than that shown in Figure D-12. Unfortunately, time constraints and lack of extra samples did not allow for rerunning of the baseline tests.

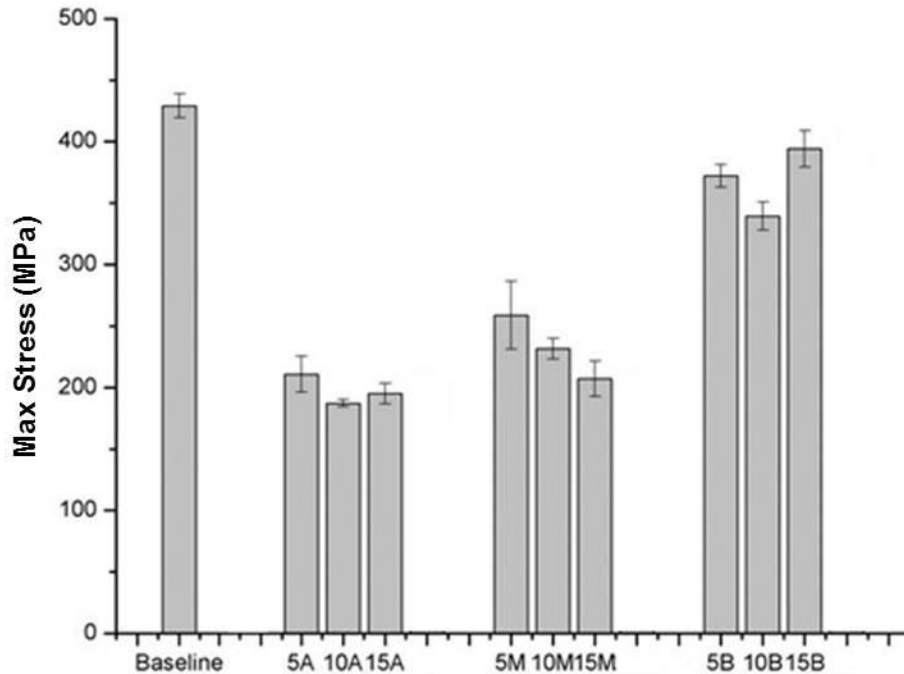


Figure D-12. Effect of aspect ratio and through-thickness location on compressive strength of test coupons

The intent of the second set of coupons was to investigate the effect of wave amplitude on compressive strength. Therefore, as shown in Table D-4, the wave defects were fabricated with a constant aspect ratio of 10 and were embedded in the middle of the coupons to keep the through-thickness location constant. A minimum of five samples for each configuration was tested. Figure D-13 shows that as the amplitude of the wave defect increased, the maximum compressive stress of the coupon specimen decreased. The compressive stresses are shown relative to the baseline sample from the first set of coupons, and the error bars represent one standard deviation. The explanation for this drop in load-carrying capacity with increasing wave amplitude is that as the amplitude increases the critical buckling load decreases. Also, because of the presence of the clamps at each end of these second-set samples, failure did not occur due to brooming but

instead due to delamination that initiated at the peak of the wave defect (Figure D-14a). For the coupons with the 1-mm amplitude defects, the failures occurred at higher loads and 45° kink bands were typically observed at failure (Figure D-14b).

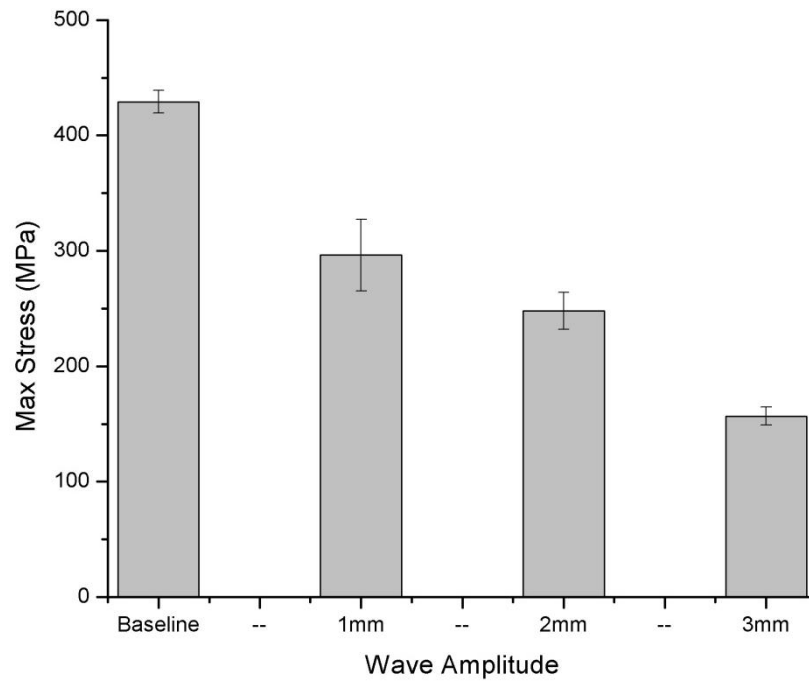


Figure D-13. Compressive strength of test coupons as a function of wave amplitude

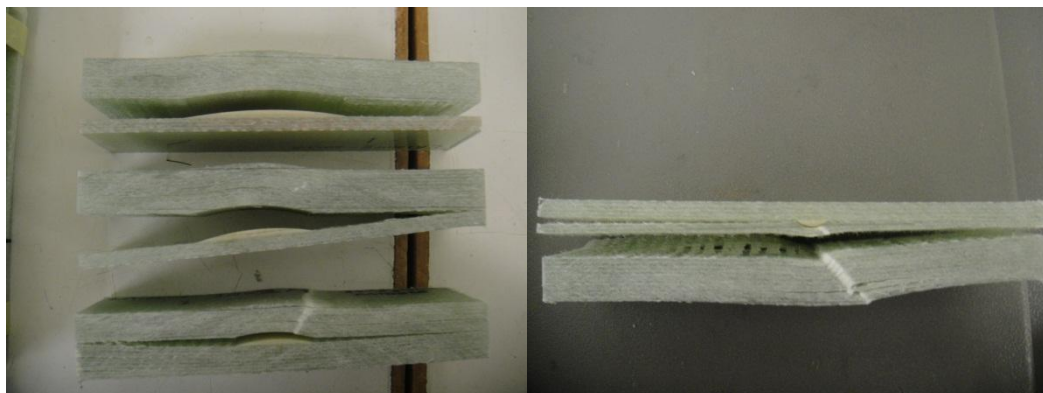


Figure D-14. Second-set coupons with (a) larger wave amplitudes failing due to delamination initiating at the top of the wave defect and with (b) smaller wave amplitudes exhibiting kink bands

3.1.1 Three-Dimensional DIC measurements

Three-dimensional DIC measurements were taken to observe how the compressive strain on the outer surface of the coupon specimens varied as a result of changes in the embedded wave defects. The presence of a wave defect induced a strain concentration, or amplification, on surface near the A-side. These strain amplifications were also likely present in the internal layers above the defect, but DIC is not able to see below the surface of the specimen. Figure D-15 shows typical strain measurements on samples with different aspect ratios during compression tests. The images show the amplification of strain on the surface in the region of the defect, and this amplification does not vary significantly with aspect ratio. More significant changes in strain amplification were observed in the DIC measurements of the coupons with varying wave amplitude, which are shown in Figure D-16. As the amplitude of the wave defect increased, the level of strain amplification visibly increased on the surface near the defect, indicating that perhaps the wave amplitude is a more critical defect parameter in terms of compressive strength than the aspect ratio.

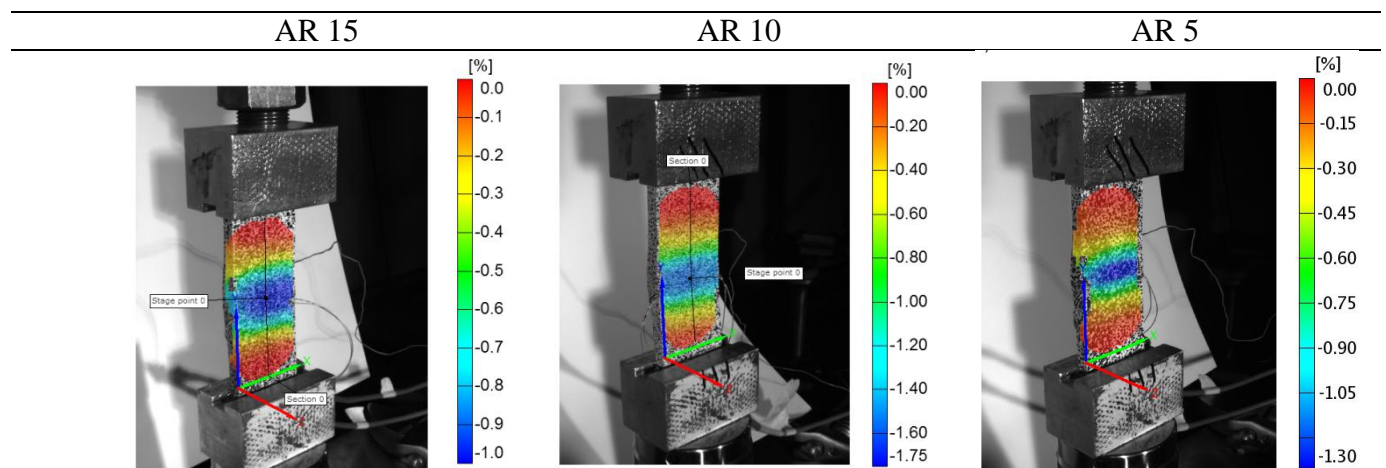


Figure D-15. Examples of DIC strain measurements during compression tests on coupon specimens with a defect amplitude of 3 mm. Note that AR denotes aspect ratio.

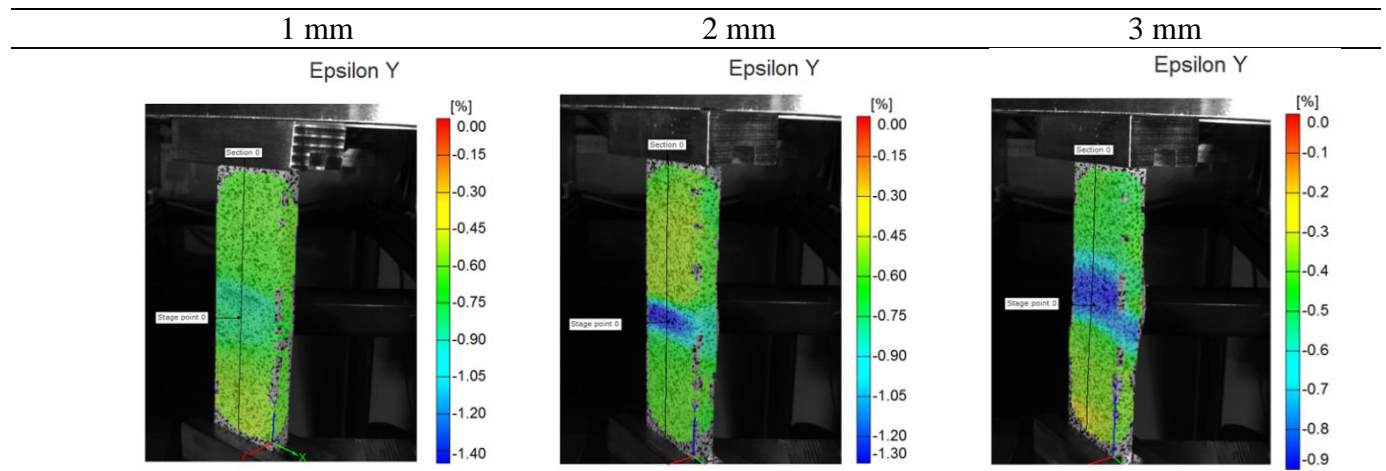


Figure D-16. Examples of DIC strain measurements during compression tests on coupon specimens with aspect ratio of 10.

3.1.2 Finite element models

To investigate the effect of only the wave-defect aspect ratio on the coupon sample compressive strength, the wave amplitude was held constant at 3 mm, and the defect was located in the middle of each finite element model. As previously described in Section 3.0, the compressive load associated with a compressive strain of 0.33% was used as the failure criterion for the finite element models. The normalized maximum compressive load for a finite element model was computed based on the ratio of the maximum load in a wave-defect free model for a max compressive strain of 0.33% to that in a wave-defect model with a max compressive strain of 0.33%. A comparison of the normalized max load as a function of aspect ratio with wave defects in the middle for the finite element models vs. experiment are shown in Figure D-17. For these particular conditions (i.e., wave defect in the middle), Figure D-12 and Figure D-17 show that the compressive strength decreased as the aspect ratio increased. However, when the defects were located near the A-side or B-side per Figure D-12, no clear trend was observed in the compressive strength as a result of an increasing aspect ratio. The finite element

model also indicated that the aspect ratio of the wave defect (in the middle) did not significantly affect the compressive strength of the coupon samples (Figure D-17).

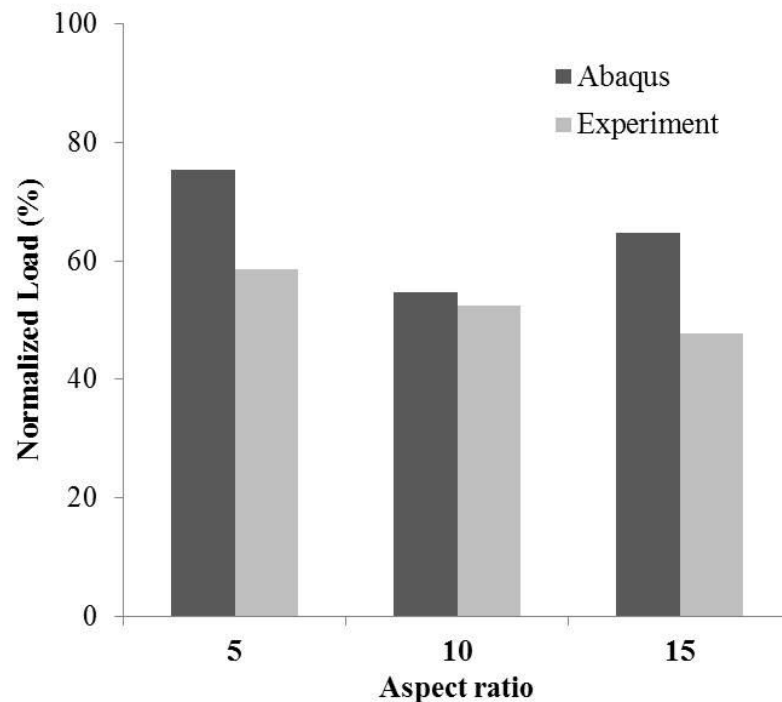


Figure D-17 Normalized maximum compressive load as a function of aspect ratio for a wave defect in the middle (FE model vs. experiment)

The first set of experimental coupons showed that the through-thickness location of an out-of-plane wave defect significantly affected the composite compressive strength (Figure D-12). Recall that defects located near the A-side resulted in the buckling of a majority of the fibers, thereby reducing the load-carrying capacity of the specimen relative to the other configurations in the study. As the defect moved away from the A-side, the compressive strength of the sample increased such that samples with defects located close to the B-side had the highest compressive strengths for the three types of wave defects. The finite element simulations agree with the experimental data, as shown in Figure D-18 where the normalized loads from the finite element models and the experiments are compared as a function of defect location.

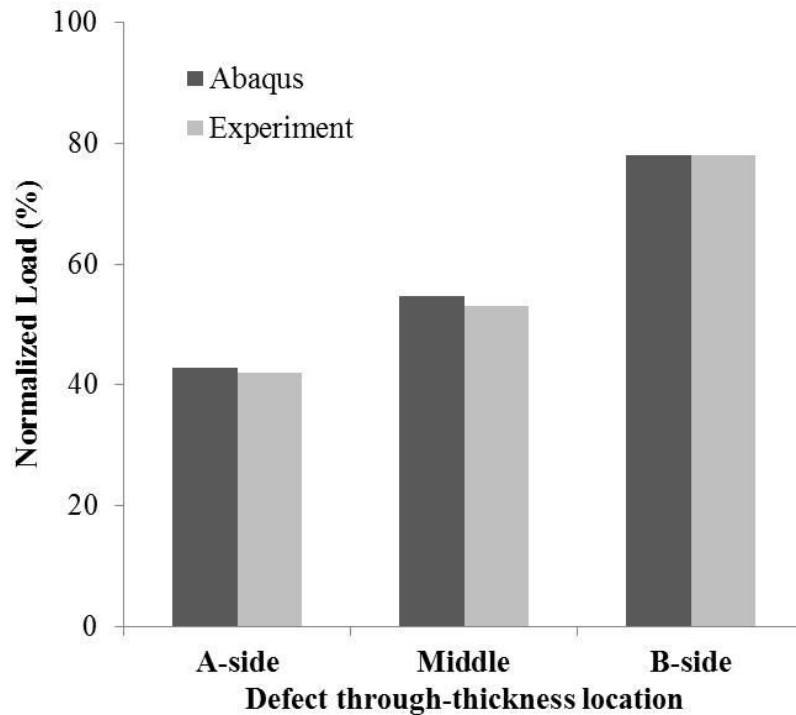


Figure D-18. Normalized maximum compressive load as a function of through-thickness location (FE model vs. experiment)

The normalized maximum loads measured experimentally compared with those of the finite element models as a function of wave amplitude for samples with defects having an aspect ratio of 10 and located in the middle are shown in Figure D-19. Similar trends were observed between the models and experiments, where the strength of the coupon samples decreased (as determined using the 0.33% strain criterion) as the amplitude of the wave defect increased. Overall, the trends observed in the finite element models correlated well with the trends observed experimentally from the two sets of coupon samples loaded in compression.

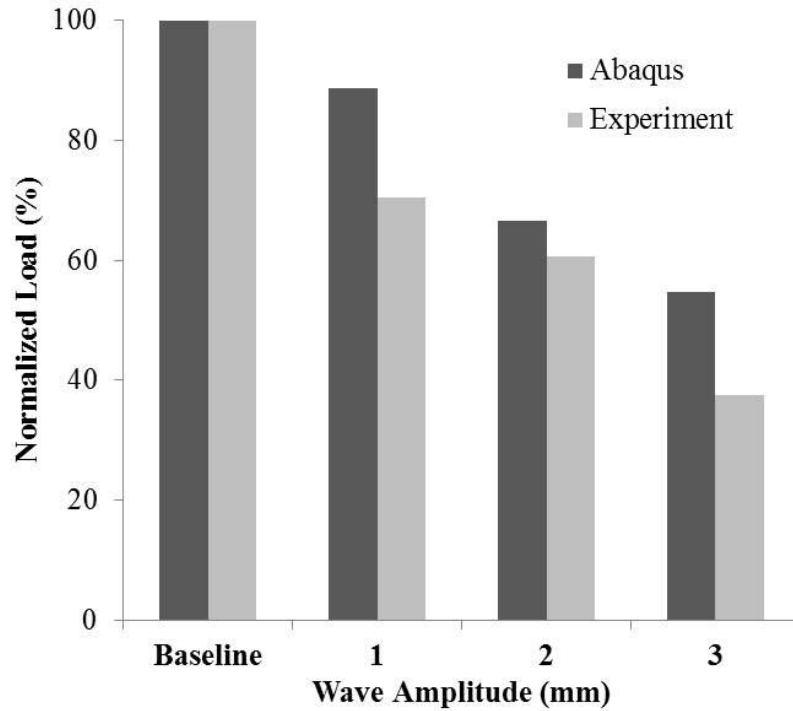


Figure D-19. Normalized maximum compressive load as a function of wave amplitude (FE model vs. experiment)

Strain contours for finite element models with the same compressive displacement, same wave-defect aspect ratio, same defect location (middle) but differing wave amplitudes are shown in Figure D-20. These contours compare well to those measured using the DIC system (Figure D-16) for the same configuration. The strain field is essentially uniformly distributed for the baseline samples except at the two ends, which is due to the boundary conditions. With the presence of a wave defect, the compressive strain is concentrated between the location of the defect and the A-side of the sample. As the amplitude of the wave defect increases, the magnitude of the amplified strain increases.

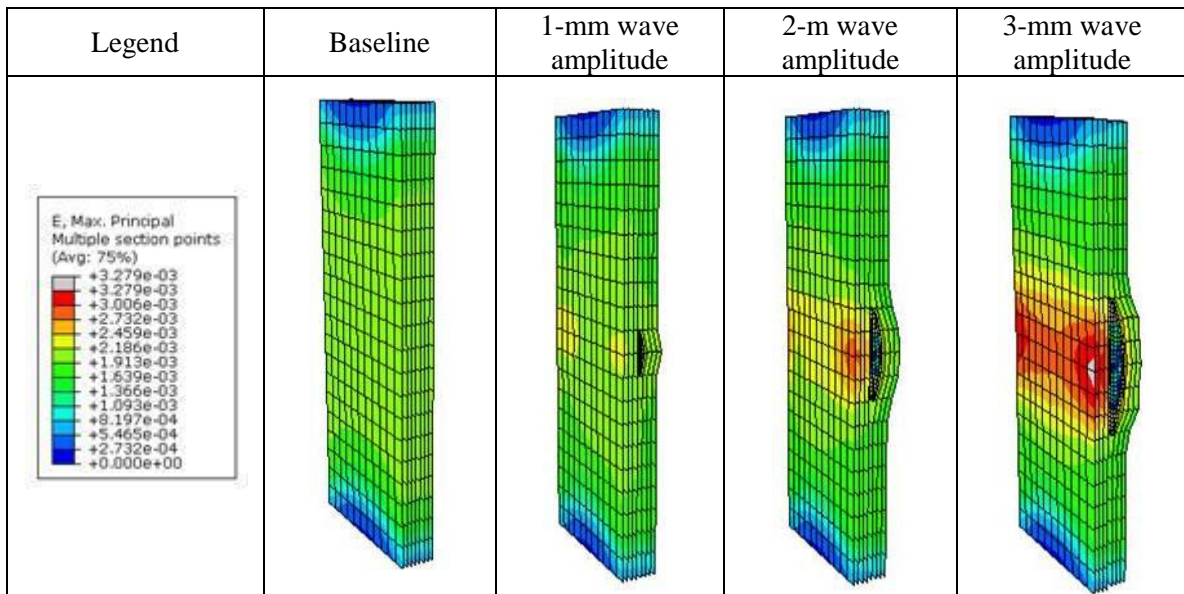


Figure D-20. Strain field distribution of samples with wave-defect aspect ratio of 10 in the middle with various amplitudes.

3.2 Fatigue Testing

Fatigue tests were performed on the third set of coupon specimens, which were cut from the nine-meter blade that had the embedded wave defects. All wave defects had the same amplitude, i.e. 3 mm. Sample 3.5HP3D-2 had a defect with an aspect ratio of 15. The DIC test results of the sample after 64k cycles at the load of 50% of maximum static-failure stress are shown in Figure D-21. The Epsilon Y vs. Load plot in Figure D-21 shows three loading and unloading cycles during the fatigue test. The three curves are indistinguishable as the strain remains linear and consistent between each load cycle.

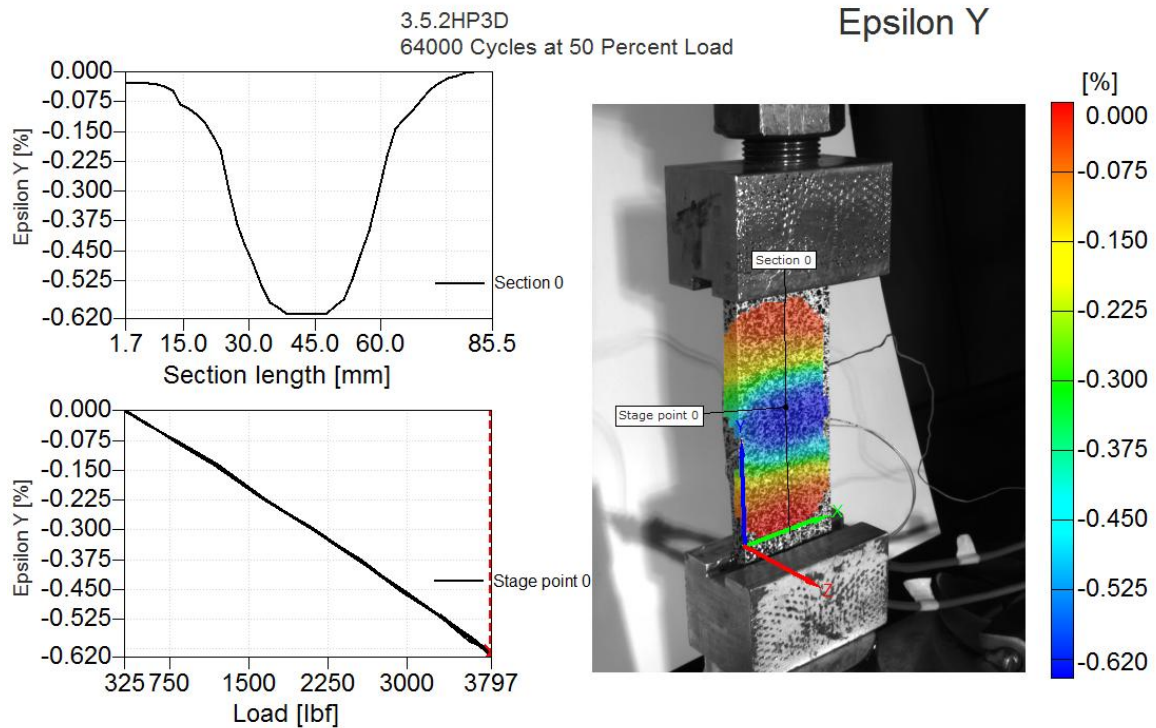


Figure D-21. Fatigue test sample at 3.5 meter location (AR 15) at 64k cycles measured at 50% max load.

The load was then raised to 70% of maximum static-failure stress. A DIC measurement was performed at this higher load level without applying a significant number of cycles. The DIC data analysis is shown in Figure D-22. Other than an expected increase in the strain magnitude, the behavior of the sample from cycle to cycle remained essentially unchanged with respect to the lower load level. Several thousand more cycles were put on the test specimen at 70% of maximum static-failure stress. The Epsilon Y vs. Load plot in Figure D-23 shows a developing hysteresis between each loading and unloading cycle as the number of cycles increased. Figure D-23 shows the strain field in the sample just prior to failure, where the strain distribution across the width of the sample is no longer uniform. Figure D-24 shows a typical out-of-plane buckling failure mode of two fatigue-test samples with different aspect ratios. The same

loading conditions were applied to samples 5.0HP3D-2 and 6.0HP3D-1 (50% for 64,000 cycles, then 70% until failure) and similar behavior was observed through the fatigue tests. The fatigue test results are summarized in Table D-6.

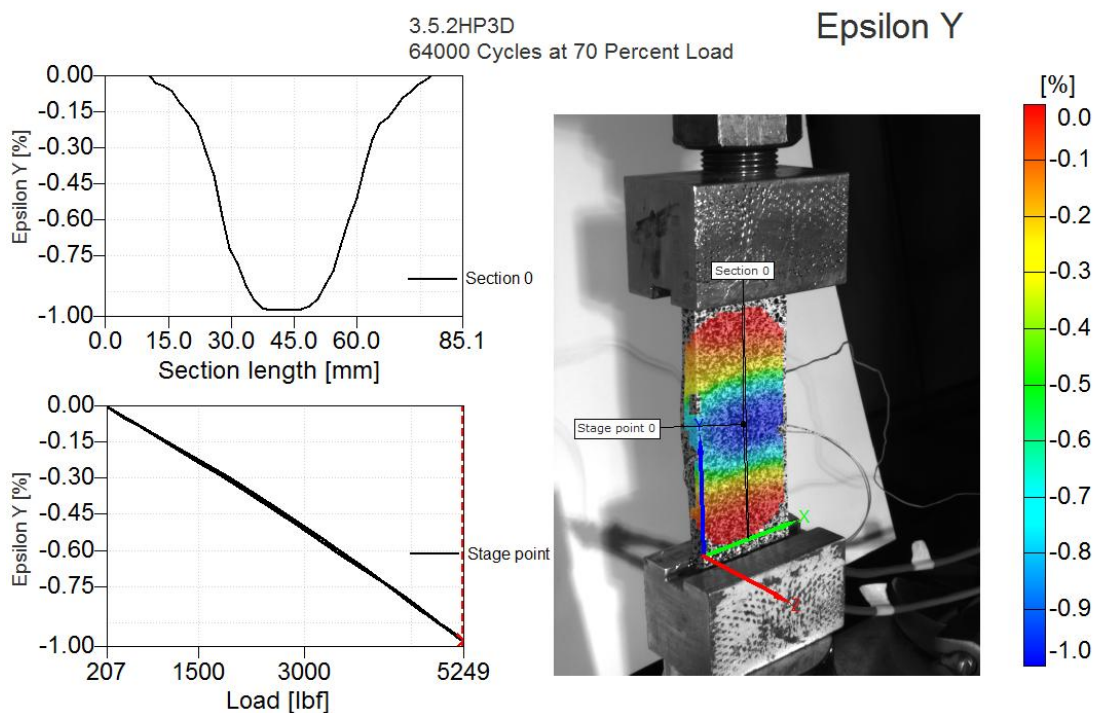


Figure D-22. Fatigue test sample at 3.5 meter location (AR 15) at 64k cycles measured at 70% max load.

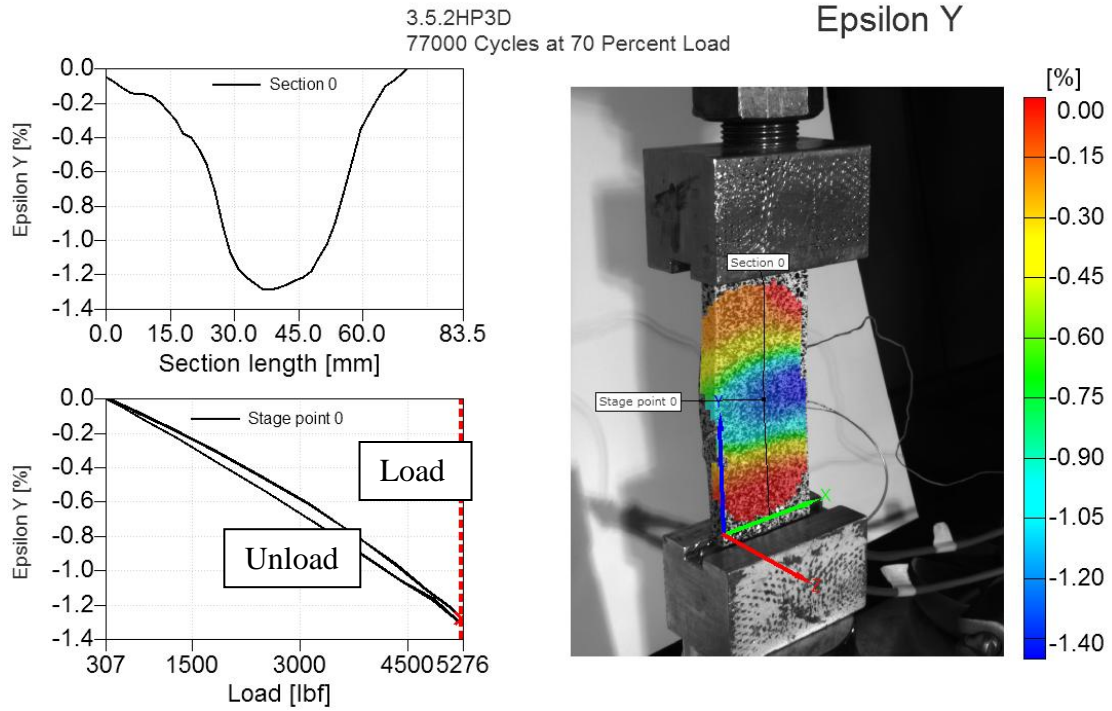


Figure D-23. Fatigue test sample at 3.5 meter location (AR 15) at 77k cycles measured at 70% max load.

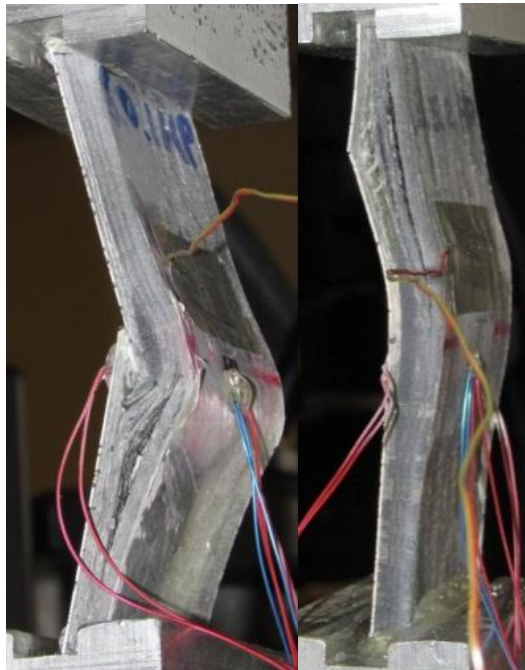


Figure D-24. Typical failure modes of third-set coupons during fatigue tests

Table D-6. Results from fatigue tests of third set of coupon specimens with 3-mm wave amplitude

Sample ID	Defect Aspect Ratio	Cycles to failure
3.5HP3D-2	15	77,000
5.0HP3D-2	10	67,950
6.0HP3D-1	5	69,340

These data show that as the aspect ratio changed from 15 to 10, the number of cycles to failure decreased. However, as the aspect ratio decreased further from 10 to 5, the number of cycles to failure increased. Sample 3.5HP3D-2 has the highest aspect-ratio defect, i.e. least amount of curvature, and lasted over 7000 cycles more than any other comparable defect. While testing of a greater quantity of samples is required to get a statically significant conclusion, a large per cent jump in cycle count may be attributed to the aspect ratio of the defect in this sample relative to the other three samples shown in Table D-6.

4 Conclusions

Composite coupons were fabricated and tested with and without pre-made out-of-plane wave defects. The dimensions of the wave defects and location within the ply stack were controlled to study the effect of defect aspect ratio, amplitude, and through-thickness location on the specimen compressive strength. The specimens were tested in compression for static and fatigue failure. Digital image correlation measurements captured the strain amplification in the region of the defects. Finite element models of the compression tests were compared to strain fields as measured with DIC, and to assist in the interpretation of the trends observed from experiments. The tests and models

indicated that wave defect amplitude and through-thickness location significantly affected the compressive strength of the coupon samples: higher wave amplitude and wave locations closer to A-side each lead to lower compressive strength; the aspect ratio shows some influence, but not as significant as defect location and amplitude. Further study is required to better understand the effect of aspect ratio.

Acknowledgements

This study was supported by the U.S. Department of Energy (Grant # DE-EE001374).

References

- [1] “2010 Wind Technologies Market Report”. U.S. Department of Energy: Energy Efficiency and Renewable Energy (EERE). June 2011.
- [2] D. Berry, “Wind Turbine Blades Blade Mfg. Improvements and Issues”, 2004 Wind Turbine Blade Workshop, Albuquerque, NM, February 24-25, <http://www.sandia.gov/wind/04Presentations.htm>, 2004.
- [3] J.F. Mandell , D.D. Samborsky, and L. Wang, “Effects of Fiber Waviness on Composites for Wind Turbine Blades”, Proceedings of the 48th International SAMPE Symposium, Long Beach, CA, pp. 2653-2678, 2003.
- [4] D. D. Samborsky, J. F. Mandell and D. S. Cairns, “Selection of Reinforcing Fabrics for Wind Turbine Blade,” Proc. 1999 ASME Wind Energy Symposium, ASME International, New York, 1999, pp. 32-42.
- [5] J. F. Mandell, D. S. Cairns, D. D. Samborsky, “Prediction of Delamination in Wind Turbine Blade Structural Details,” Journal of Solar Energy Engineering, Vol. 125/529, Nov 2003.
- [6] D.S. Cairns, L. McKittrick, D. Rabern , D. Vanluchene, J.F. Mandell, “Design and Manufacturing Synthesis of Composite Wind Turbine Blades,” 1999 ASME Wind Energy Symposium Collection of Papers, Reno, NV, January, 1999, pp 58-65.
- [7] D.S. Cairns, A. Sears, J.F. Mandell, and L.R. McKittrick, “Design Considerations for Buckling of Composite Wind Turbine Blades,” 2000 ASME Wind Energy Symposium Collection of Papers, Reno, NV, January, 2000, pp 375-393.

- [8] D.S. Cairns, J. Skramstad, "Manufacturing Process Evaluations for Composite Wind Turbine Blades," Proceedings of SAMPE 2000, May 2000.
- [9] D.S. Cairns, D.D. Samborsky, and J.F. Mandell, "Resin Transfer Molding in Composite Wind Turbine Blade Structures," 2001 ASME Wind Energy Symposium Collection of Papers, Reno, NV, January, 2001, pp 38-48.
- [10] D. S. Cairns, J. F. Mandell, and D. D. Samborsky, "Quantification of Processing Parameters for Wind Turbine Blades," ASME Wind Energy Symposium Collection of Papers, paper no. AIAA-2003-0694, January, 2003, pp 181-191.
- [11] D. Berry: "CX-100 Manufacturing Final Project Report", Sandia National Laboratories, November 2007.
- [12] B. LeBlanc, C. Niezrecki, P. Avitabile, J. Chen, and J. Sherwood, "Full-field Inspection of a Wind Turbine Blade Using Three-dimensional Digital Image Correlation", Proc. SPIE 7979, 79790L (2011).
- [13] A. Puri, J.P. Dearl, A. Morris, and F.M. Jensen, "Analysis of Wind Turbine Material using Digital Image Correlation", Proceedings of the 11th SEM International Congress and Exposition, Orlando, Florida, 2008.
- [14] D. Jauffrès, J.A. Sherwood, C.D. Morris, and J. Chen, "Discrete Mesoscopic Modelling for the Simulation of Woven-Fabric Reinforcement Forming," International Journal of Material Forming, (2009)
- [15] K. Fetfatsidis, J. Sherwood, "Simulation of the Manufacturing of Non-Crimp Fabric Composite Wind Turbine Blades to Predict the Formation of Wave Defects," Proceedings of the 14th ESAFORM Conference, Belfast, United Kingdom, 2011
- [16] K. Fetfatsidis, J. Sherwood, D. Winchester, D. Jauffrès, P. Avitabile, J. Chen, "Using Modal Analysis to Investigate the Validity of Finite Element Models for Simulating the Thermoforming of Woven-Fabric Reinforced Composites," Proceedings of the 13th ESAFORM Conference, Brescia, Italy, 2010
- [17] D. Adams, and S. Bell, "Compression strength reductions in composite laminates due to multiple-layer waviness," Composites Sci. and Tech., Vol. 53 (1995).
- [18] H.M. Hsaio, and I.M. Daniel, "Effect of fiber waviness on stiffness and strength reduction of unidirectional composites under compressive loading," Composites Sci. and Tech., Vol. 56 (1996).
- [19] K.J. Chun, and I.M. Daniel, "Effects of material and geometric nonlinearities on the tensile and compressive behavior of composite materials with fiber waviness," Composites Sci. and Tech., 61 (2001).

- [20] M. R. Piggot and B. Harris, "Factors Affecting the Compression Strength of Aligned Fiber Composites," *Advances in Composite Materials, Proceedings, Third International Conference on Composite Materials, Paris, France, Vol. 1, 1980*, pp. 305-331.
- [21] D. Adams, "Effects of Layer Waviness on the Compression Strength of Thermoplastic Composite Laminates," *Journal of Reinforced Plastics and Composites*, Vol. 12, April 1993, pp. 415-429
- [22] D. Adams and M. W. Hyer, "Effects of Layer Waviness on the Compression Response of Laminates," *Compression Response of Composite Structures, ASTM STP 1185, 1994*, pp.65-77.
- [23] D. Adams and M. Hyer, "Analysis of Layer Waviness in Flat Compression-Loaded Thermoplastic Composite Laminates," *Journal of Engineering Materials and Technology*, January 1996, Vol.118, pp.63-70.
- [24] E. T. Camponeschi, Jr., "Compression of Composite Materials: A Review," *Composite Materials: Fatigue and Fracture, ASTM STP 1110, Third Volume*, pp.550-578.